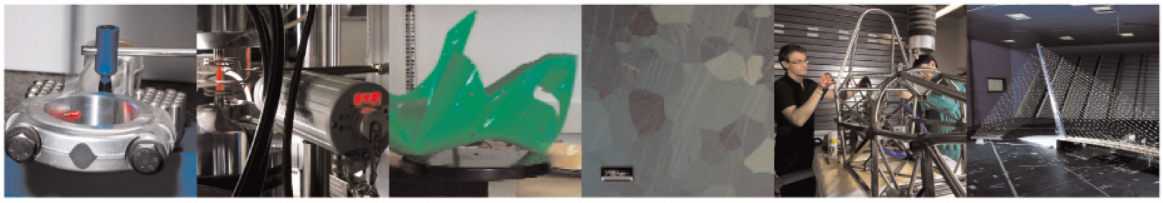

Enhancement of the broadband vibration attenuation of a resistive piezoelectric shunt

M. Berardengo, S. Manzoni, M. Vanali, R. Bonsignori

This is a post-peer-review, pre-copyedit version of an article published in *Journal of Intelligent Material Systems and Structures*. The final authenticated version is available online at: http://dx.doi.org/10.1177/1045389X20988090

DIPARTIMENTO DI MECCANICA ■ POLITECNICO DI MILANO
via G. La Masa, 1 ■ 20156 Milano ■ EMAIL (PEC): pecmecc@cert.polimi.it
http://www.mecc.polimi.it
Rev. 0

Enhancement of the broadband vibration attenuation of a resistive piezoelectric shunt

M. Berardengo[1], S. Manzoni[2], M. Vanali[3], R. Bonsignori[2]

1. Università degli Studi di Genova - Department of Mechanical, Energy, Management and Transportation Engineering

   Via Opera Pia, 15A - 16145 Genoa (Italy)

2. Politecnico di Milano – Department of Mechanical Engineering

   Via La Masa, 34 – 20156 Milan (Italy)

3. Università degli Studi di Parma - Department of Engineering and Architecture

   Parco Area delle Scienze, 181/A – 43124 Parma (Italy)

Corresponding author: S. Manzoni (stefano.manzoni@polimi.it)

ABSTRACT

This paper shows how to enhance the vibration attenuation obtained by means of piezoelectric resistive shunt coupled to the use of negative capacitances. This improvement is achieved by adding an inductance in the shunt circuit. This additional inductance is not used to the usual purpose of mono-modal control, but to improve the attenuation in a broader frequency range.

The benefits offered by the use of the inductance are explained by describing the shunted electro-mechanical system as a feedback control loop. The achievable attenuation improvements are highlighted in the paper at first through numerical analyses and then by means of an experimental campaign which also allows to evidence the reliability of the model employed to describe the electro-mechanical system.

KEYWORDS: piezoelectric shunt, resistive shunt, inductive shunt, negative capacitance, broadband control, vibration

1 Introduction

The use of piezoelectric shunt is a well-established technique for vibration control in light structures, where the piezoelectric transducer acts at the same at time as a sensor and an actuator. One of the most attractive features of this approach is that it is inexpensive because neither digital systems nor feedback sensors are needed. Different vibration problems have been already shown to be successfully solved with this type of approach (e.g. (Sun et al., 2009; Xie et al., 2019; Zhou et al., 2014)).

Piezoelectric shunt relies on the electrical connection between a piezoelectric actuator (or even more than one) bonded to the vibrating structure and a properly designed electric impedance. According to the type of control required, a different type of electric impedance is employed: LR impedances (i.e. either series or parallel of a resistance *R* and an inductance *L*, also named resonant shunt) for single mode control (Hagood and Flotow, 1991; Høgsberg and Krenk, 2015; Matveenko et al., 2018; Soltani et al., 2017; Thomas et al., 2012; Yamada et al., 2010), resistive impedances (i.e. impedances constituted by a single resistance *R*) for single mode control (Hagood and Flotow, 1991; Thomas et al., 2012) as well as for broadband control, and multi-branch impedances for multi-mode control (e.g. (Behrens et al., 2003b; Berardengo et al., 2017a; Darleux et al., 2020; Dell'Isola et al., 2004; Lossouarn et al., 2018; Raze et al., 2020; Wu, 1996)).

When two or few modes in a limited frequency band need to be controlled, the multi-branch networks still represent the best solution in terms of attenuation. However, it has been shown that the resistive shunt can represent a good alternative solution. Indeed, although the resistive shunt usually provides low attenuation levels (Thomas et al., 2012), its performances can be much improved by adding a negative capacitance (NC) $-C$ in the shunt circuit (Beck et al., 2013; Berardengo et al., 2017b, 2016c, 2015b; Caruso, 2001; de Marneffe and Preumont, 2008; Heuss et al., 2016; Neubauer et al., 2006; Park and Baz, 2005; Park and Inman, 2003; Pohl, 2017). Moreover, since it is more robust to possible mistuning than the multi-branch impedances and mistuning often occurs in real applications (Andreaus and Porfiri, 2007; Berardengo et al., 2016b, 2015a) (e.g. due to thermal shifts), when two or more modes must be damped, the resistive shunt coupled to the use of NCs (RNC shunt in the following) can be considered as a very attractive solution which offers high performances, high robustness and ease of implementation (e.g. (Behrens et al., 2003a; Berardengo et al., 2016c; Bricault et al., 2019)). In light of this, the RNC shunt will be the main focus of this paper.

Particularly, the aim of the present paper is to show how to improve the attenuation provided by an RNC shunt on a given frequency range by modifying the shunt impedance (which is a topic addressed also in other works (Berardengo et al., 2016a; Oshmarin et al., 2019) in the literature), more specifically by adding an inductance in the shunt circuit. While an inductor is usually used for mono-modal control, here it is used to the aim of improving the broadband attenuation provided by the RNC shunt. The paper is structured as follows: at first, the model used to describe the piezoelectric shunt is presented and it is shown that the electric part of the electro-mechanical system (EMS, composed by the vibrating structure, the piezoelectric transducer and the shunt impedance) can be seen as a controller. Thus, the whole EMS is described as a mechanical system controlled through a feedback loop. This model puts the basis to explain how to increase the attenuation provided by the RNC with the addition of an inductance in the shunt circuit. Then, some numerical examples to evidence the benefits of the proposed method are presented and rules for the tuning of the inductance value are provided. Finally, the theory is validated by means of experiments.

2 Model of the EMS

The model used herein was proposed by Thomas et al. (Thomas et al., 2012) and refined by Berardengo et al. (Berardengo et al., 2016c), and it is briefly recalled here to allow the description of the shunted EMS as a feedback loop. Consider an external force *F* exciting a generic elastic structure with a piezoelectric patch bonded to it and shunted by means of a generic electric impedance *Z* (Figure 1a). *Q* is the charge in the upper electrode (-*Q* in the lower electrode) and *V* is the voltage between the electrodes. The displacement response *U* at any generic point *x* of the structure and time *t* can be described by means of a modal model, relying on the modal coordinates q_i (with $i = 1, \dots, N$, being *N* the number of modes of the system;

theoretically $N \to \infty$) and the eigenvectors Φ_i (scaled to the unit modal mass) of the structure with the piezoelectric actuator in short-circuit (i.e. $Z = 0$). The modal coordinates are the solutions of the following problem (Ducarne et al., 2012; Thomas et al., 2012, 2009):

$$\ddot{q}_i + 2\xi_i\omega_i\dot{q}_i + \omega_i^2 q_i - \chi_i V = F_i \qquad i = 1, \dots, N \tag{1}$$

$$C_\infty V - Q + \sum_{i=1}^{N} \chi_i q_i = 0 \tag{2}$$

where ω_i is the *i*th eigenfrequency of the EMS in short-circuit, ξ_i is the associated non-dimensional damping ratio and F_i is the modal force. C_∞ is the electrical capacitance of the piezoelectric patch with blocked structure, which also corresponds to the value of the capacitance at infinite frequency (Berardengo et al., 2016c). χ_i is a modal coupling coefficient which describes the energy transfer between the piezoelectric patch and the *i*th mode. The term χ_i couples Eq. (1), which describes the equations of motion of the system, to Eq. (2) which describes the electric behaviour of the EMS (see Figure 1b; in this figure the term $\sum_{i=1}^{N} \chi_i \dot{q}_i$ is abbreviated as $\dot{Q}_{\mathrm{cs}}$; the dot indicates the first derivative with respect to time). The terms χ_i can be found analytically (Ducarne et al., 2012), through a finite element model (Thomas et al., 2009), or experimentally by measuring the effective coupling coefficients associated to each mode (Berardengo et al., 2018).

If only the first *n* modes out of *N* are considered, Eq. (2) can be written as:

$$C_{\mathrm{p}n} V - Q + \sum_{i=1}^{n} \chi_i q_i = 0 \tag{3}$$

where $C_{\mathrm{p}n}$ (named modal capacitance of the *n*-th mode) can be roughly seen as the value of the capacitance of the piezoelectric patch between the n^{th} and $(n+1)^{\mathrm{th}}$ modes. The use of $C_{\mathrm{p}n}$ allows to take into consideration the electrical contribution of the out-of-band modes (i.e. the modes higher than the n^{th}) in the frequency range considered. More details about the definition of $C_{\mathrm{p}n}$ and its estimation can be found in (Berardengo et al., 2018, 2016c; Toftekaer and Hogsberg, 2019). Using this reduced model, the electrical schematic of Figure 1b must be modified using $C_{\mathrm{p}n}$ in place of C_∞.

For the generic *i*-th mode, it is possible to define the modal electro-mechanical coupling factor k_i, that is a function of the modal coupling coefficient χ_i and, thus, it is a measure of the efficiency of the energy transfer between the *i*-th mode and the electric circuit and vice versa. k_i is usually estimated by estimating the short- and open-circuit eigenfrequencies:

$$k_i^2 = \frac{\chi_i^2}{\omega_i^2 C_{\mathrm{p}i}} \cong \frac{\widehat{\omega}_i^2 - \omega_i^2}{\omega_i^2} \tag{4}$$

where $\widehat{\omega}_i$ is the *i*th eigenfrequency of the EMS with the piezoelectric actuator open-circuited.

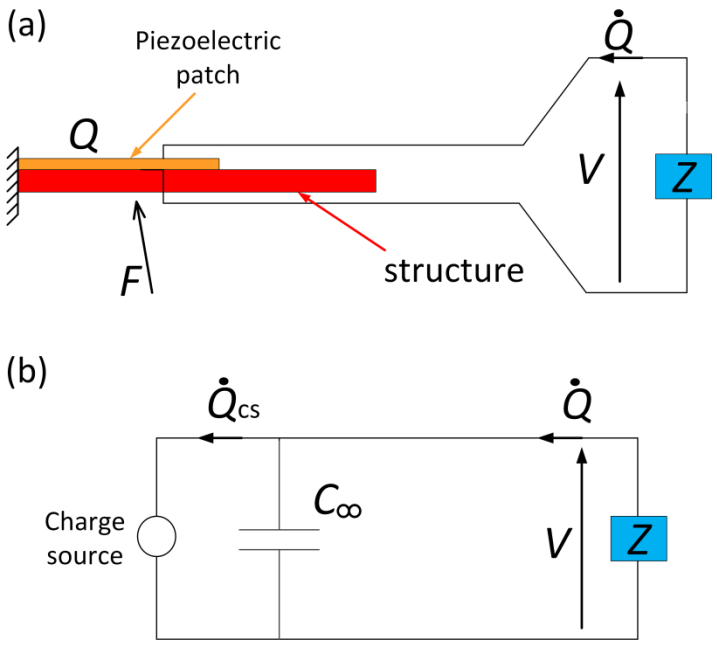

Figure 1: A generic EMS (a) and its electrical model (b)

In order to represent the behaviour of the EMS shunted with a generic impedance *Z*, the reduced model can be used. Substituting the relation linking the voltage and the charge at the piezoelectric terminals $V = -Z\dot{Q}$ and Eq. (3) in Eq. (1) where only *n* out of *N* modes are considered, the shunted EMS can be represented in the Laplace domain (*s* is the Laplace variable) by means of a feedback loop (as shown by Figure 2). Using this model, three different types of transfer function are highlighted, which will be useful to analyse the EMS behaviour: the one between the modal coordinate and the modal force, $H_{\mathrm{F}i}(s)$, that between the modal coordinate and the voltage across the piezoelectric electrodes, $H_{\mathrm{V}i}(s)$, and the controller transfer function $K_{\mathrm{t}}(s)$:

$$H_{\mathrm{F}i}(s) = \frac{q_i(s)}{F_i(s)} = \frac{1}{s^2 + 2s\xi_i\omega_i + \omega_i^2} \tag{5}$$

$$H_{\mathrm{V}i}(s) = \frac{q_i(s)}{V(s)} = \frac{\chi_i}{s^2 + 2s\xi_i\omega_i + \omega_i^2} \tag{6}$$

$$K_{\mathrm{t}}(s) = \frac{V(s)}{Q_{\mathrm{cs}}(s)} = \frac{-Z(s)s}{1 + Z(s)C_{\mathrm{pn}}s} \tag{7}$$

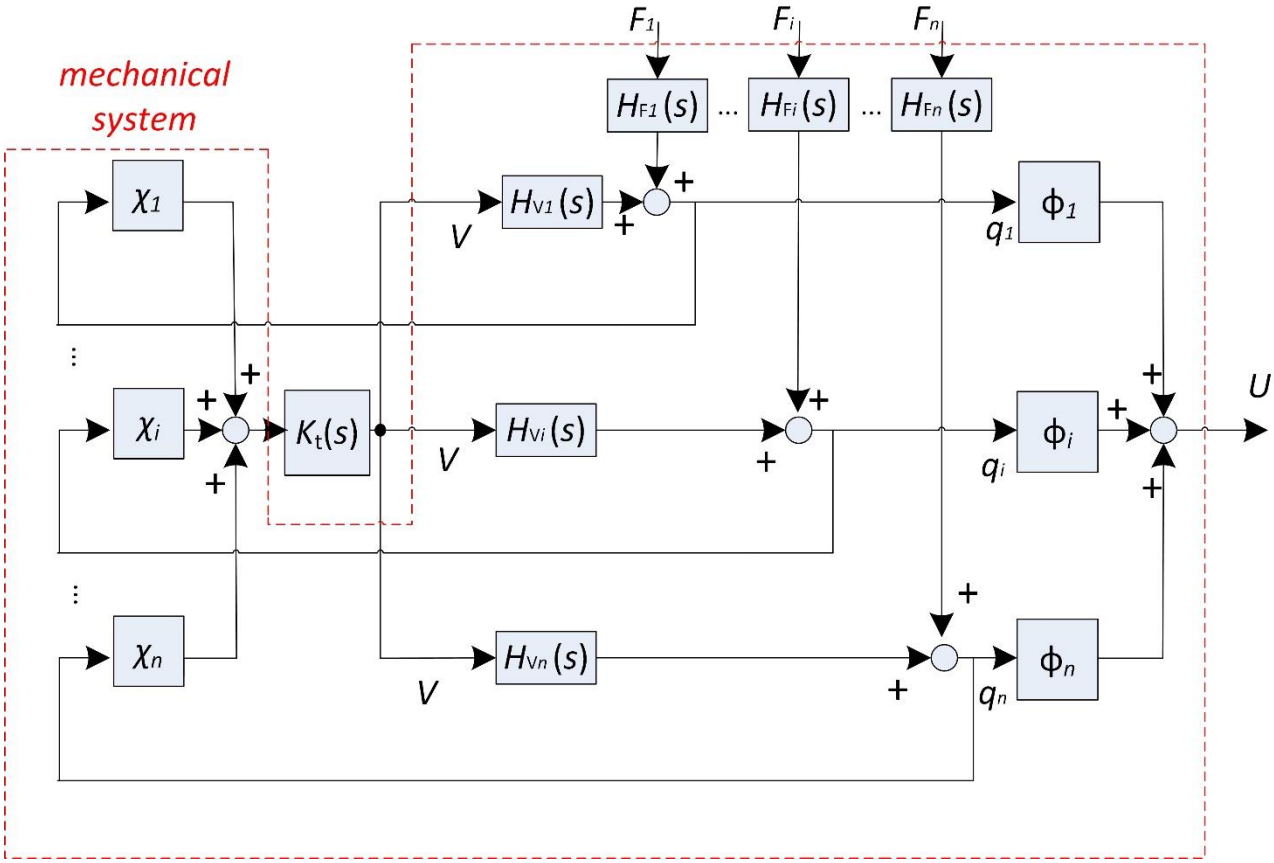

Figure 2: Feed-back representation of the piezoelectric shunt.

The obtained representation of the shunted EMS as a feedback control loop is in agreement with other EMS models (Moheimani and Fleming, 2006; Moheimani et al., 2003). Here, this new model has been proposed since those already available in the literature allow to focus the analysis on the voltage at the terminals of the piezoelectric actuator *V*, while the proposed one allows to focus on the relation between the EMS displacement *U* and the forcing term *F*, thus enabling to evidence straightforwardly the effects of the controller on the target variable.

As shown by Figure 2, the controller is represented by K_t and it depends on the shunt impedance *Z* (see Eq. (7)). This representation is very useful since it allows to understand the effect of the shunt impedance by studying the frequency response function (FRF) of the controller. In this way, it is possible to understand why an LR impedance coupled to an NC (LRNC shunt in the following) provides higher attenuation than an RNC shunt in case of mono-modal control and why the RNC shunt is theoretically able to work on an extended frequency range. Indeed, Figure 3 shows the FRF (obtained replacing the Laplace variable *s* with jω in Eq. (7), where j is the imaginary unit and ω is the circular frequency) of the optimal controller K_t for an LRNC impedance (with the three elements connected in series) tuned for mono-modal control (using the tuning formulations provided in (Berardengo et al., 2018)) and for an RNC impedance (with the elements connected in series) tuned again for mono-modal control (employing the tuning formulation provided in (Berardengo et al., 2016c)). The eigenfrequency of the mode to be controlled by the two shunts was set equal to 100 Hz, as an example. From Figure 3, it is possible to notice that the controller FRF shows a peak when an LRNC impedance is employed. This peak, generated by the addition of the inductance, is due to the occurrence of an additional eigenfrequency in the system (Thomas et al., 2012). Therefore, thanks to the introduction of this additional resonance, the magnitude of the controller FRF at 100 Hz is much higher

for the LRNC impedance than for the RNC impedance, thus explaining the higher attenuation performance of the resonant shunt at the target frequency (i.e. 100 Hz in this case). Conversely, the phase of K_t for the RNC impedance is closer to -90° (which is the optimal phase value for this control (Preumont, 2002)) in a wide frequency range than for the LRNC impedance, explaining the broadband control capability of the RNC shunt.

Starting from these considerations, the aim of the newly proposed shunt impedance is to work on the shape of the K_t transfer function trying to preserve the increase of the controller gain provided by the use of an inductance in the shunt circuit, while keeping the phase of K_t as close as possible to its optimal value on a wide frequency range. In the following, the paper will explain that this result can be achieved by a proper tuning of the inductance value. However, before addressing the tuning strategy, it is needed to discuss how to assure the stability of the EMS. Indeed, being the NC a device built employing operational amplifiers and with an active nature, instability can occur.

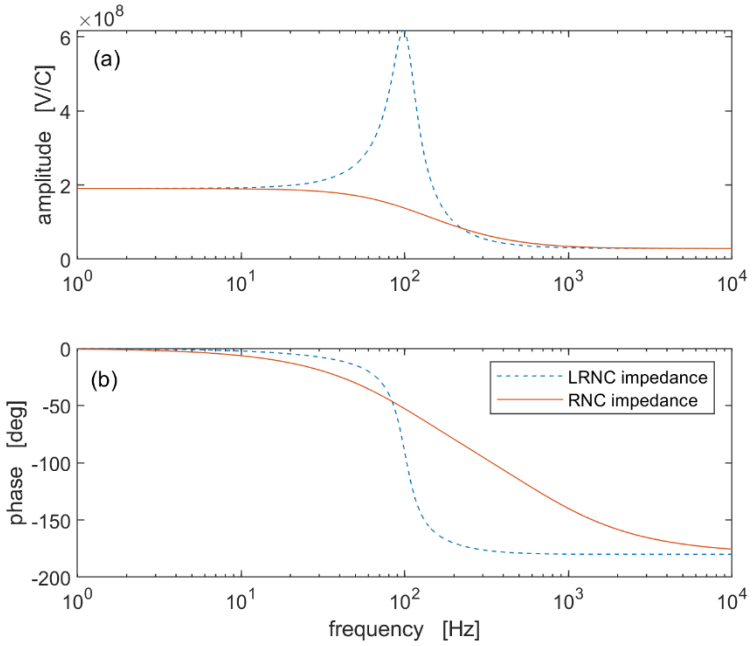

Figure 3: FRF of K_t for an LRNC impedance and an RNC impedance: amplitude (a) and phase (b). The mechanical system to be controlled is assumed to be a single-degree-of-freedom system with k_i=0.1, ω_i=2π·100 rad/s, C_{p1}=35 nF and C/C_{p1}=1.1.

2.1 FRF of the EMS and stability

In order to check the conditions which guarantee the stability of the EMS, an approach similar to that proposed in (Berardengo et al., 2016c) is used. The stability is analysed mode by mode of the EMS. Then, the stability of the whole EMS is governed by the strictest condition among those on all the modes. To do so, a single-degree-of-freedom approximation is considered, which is valid in case of low modal density. Keeping only the i^{th} mode in the modal reduction (see Equations (1) and (2)), the behaviour of the EMS can be described for $\omega \simeq \omega_i$ as (Berardengo et al., 2017b, 2016c; Thomas et al., 2012):

$$\ddot{q}_i + 2\xi_i\omega_i\dot{q}_i + \omega_i^2 q_i - \chi_i V = F_i \tag{8}$$

$$C_{pi}V - Q + \chi_i q_i = 0 \tag{9}$$

Rearranging Equation (8) using Equation (9) and knowing that $V = -Z\dot{Q}$, the expression of the transfer function $H_i = q_i/F_i$ is found. The formulation of H_i depends on the connection among the impedance components. Indeed, the NC, *R* and *L* can be connected either in series or parallel, thus leading to the four possible impedance layouts shown in Figure 4. The analytical expression of H_i for all the four layouts is given in Table 1 and the expressions of all the symbols in the table are provided in Table 2. The application of the Routh-Hurwitz criterion (Hurwitz, 1895; Routh, 1877) to H_i allows to find the stability conditions, which are gathered in Table 3 (here, C_0 is the value of the capacitance of the piezoelectric actuator at the null frequency; the following relations hold $C_0 > C_{\mathrm{p}i} > C_\infty$). Actually, these stability conditions were computed by assuming $\xi_i = 0$ in order to obtain simple analytical expressions. However, numerical simulations showed that a non-null value of ξ_i does not change the results. The conditions of Table 3 are equal to those of a resistive shunt coupled to an NC, that means that the addition of *L* does not involve any benefit/drawback in terms of stability thresholds. More details on the stability of the EMS can be found in (Berardengo et al., 2018, 2016c) and also in (de Marneffe and Preumont, 2008).

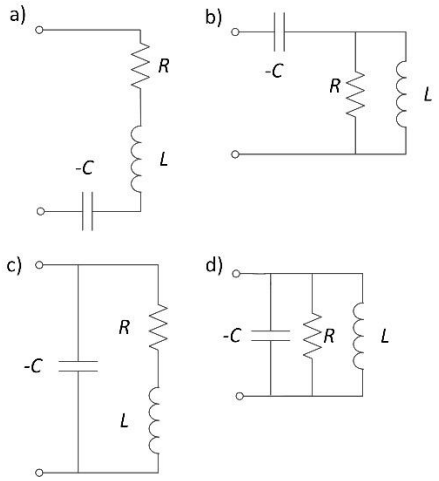

Figure 4: Possible types of circuit: type 1 (a), type 2 (b), type 3 (c), and type 4 (d).

Table 1: Expression of $H_i(s)$ for the four types of shunt circuits

Circuit Type	Expression of $H_i(s)$
1 and 3	$\dfrac{s^2 + 2s\xi_{\mathrm{e}}\omega_{\mathrm{e}} + \omega_{\mathrm{e}}^2}{s^4 + s^2\left[\omega_{\mathrm{e}}^2 + 4\xi_{\mathrm{e}}\xi_i\omega_{\mathrm{e}}\omega_i + \left(\omega_i^{\mathrm{oc}}\right)^2\right] + \omega_{\mathrm{e}}^2\left(\omega_i^{\mathrm{sc}}\right)^2 + 2s[\xi_{\mathrm{e}}\omega_{\mathrm{e}}\left(s^2 + \left(\omega_i^{\mathrm{oc}}\right)^2\right) + \xi_i\omega_i(s^2 + \omega_{\mathrm{e}}^2)]}$
2 and 4	$\dfrac{s^2 + 2s\xi_{\mathrm{e}}\omega_{\mathrm{e}} + \omega_{\mathrm{e}}^2}{s^4 + s^2\left[\omega_{\mathrm{e}}^2 + 4\xi_{\mathrm{e}}\xi_i\omega_{\mathrm{e}}\omega_i + \left(\omega_i^{\mathrm{oc}}\right)^2\right] + \omega_{\mathrm{e}}^2\left(\omega_i^{\mathrm{sc}}\right)^2 + 2s[\xi_{\mathrm{e}}\omega_{\mathrm{e}}\left(s^2 + \left(\omega_i^{\mathrm{sc}}\right)^2\right) + \xi_i\omega_i(s^2 + \omega_{\mathrm{e}}^2)]}$

Table 2: Definition of symbols

Circuit type	ω_{e}	ξ_{e}	ω_i^{oc}	ω_i^{sc}	C_{eq}	$\tilde{k}_i$
1	$\sqrt{\frac{1}{LC_{\mathrm{eq}}}}$	$\frac{R}{2}\sqrt{\frac{C_{\mathrm{eq}}}{L}}$	$\omega_i\sqrt{1+k_i^2}$	$\omega_i\sqrt{1-\frac{C_{\mathrm{p}i}}{C}\tilde{k}_i^2}$	$\frac{CC_{\mathrm{p}i}}{C-C_{\mathrm{p}i}}$	$k_i\sqrt{\frac{C}{C-C_{\mathrm{p}i}}}$
2	$\sqrt{\frac{1}{LC_{\mathrm{eq}}}}$	$\frac{1}{2R}\sqrt{\frac{L}{C_{\mathrm{eq}}}}$	$\omega_i\sqrt{1+k_i^2}$	$\omega_i\sqrt{1-\frac{C_{\mathrm{p}i}}{C}\tilde{k}_i^2}$	$\frac{CC_{\mathrm{p}i}}{C-C_{\mathrm{p}i}}$	$k_i\sqrt{\frac{C}{C-C_{\mathrm{p}i}}}$
3	$\sqrt{\frac{1}{LC_{\mathrm{eq}}}}$	$\frac{R}{2}\sqrt{\frac{C_{\mathrm{eq}}}{L}}$	$\omega_i\sqrt{1+\tilde{k}_i^2}$	ω_i	$C_{pi}-C$	$k_i\sqrt{\frac{C_{pi}}{C_{pi}-C}}$
4	$\sqrt{\frac{1}{LC_{\mathrm{eq}}}}$	$\frac{1}{2R}\sqrt{\frac{L}{C_{\mathrm{eq}}}}$	$\omega_i\sqrt{1+\tilde{k}_i^2}$	ω_i	$C_{pi}-C$	$k_i\sqrt{\frac{C_{pi}}{C_{pi}-C}}$

Table 3: Stability conditions

Circuit Type	Stability condition
1 and 2	$C > C_0$
3 and 4	$C < C_\infty$

3 The LRNC shunt

This section shows how the addition of an inductance *L* in an RNC shunt circuit is able to improve the attenuation level in a given frequency range, whose extent depends on the layout of the circuit used (see Figure 4) and on the value of the inductance added in the circuit.

In order to show the driving idea behind this type of control circuit, the problem will be analysed at first from the controller point of view, showing what occurs when a resistive and a resonant shunt (both coupled to an NC) are employed (see the first following subsection) and, thus, evidencing how the addition of *L* modifies the controller FRF providing attenuation improvements in different frequency bands and of different extent as functions of the *L* value.

Then, the second and third subsections will show, by means of numerical analyses and examples, how to set the inductance value to maximise the improvement of the control performance.

Before discussing the mentioned points, it is also noticed that the same strategy of adding an inductance with a proper value is also able to enhance the vibration attenuation performance in case of a pure resistive shunt (i.e. without NCs in the shunt circuit). However, this paper focuses on the RNC shunt because it provides attenuation performances much higher than the pure resistive shunt.

3.1 Enhancement of the performance of the RNC shunt

In order to show the benefits provided by the addition of an inductance in the RNC shunt circuits, consider the FRF of the controller K_t when, for example, a mode at about 100 Hz must be attenuated and an NC in series is used and set equal to 1.25 times C_∞ (such a value is chosen so that it also assures the EMS stability,

see previously). Figure 5 shows the FRF of K_t when an RNC shunt is used and the resistance is optimised by following the usual criterium for resistive shunt employing the formulations provided in (Berardengo et al., 2016c). The other curves reported in the figure show the trend of K_t when an inductance is added in series to the NC, $-C$, and *R* (see Figure 4a). It can be noticed that the introduction of *L* increases the K_t magnitude of the RNC (red solid thin curve) case in a given frequency range whose width depends on the *L* value. Considering the phase, it can be noticed that there is a frequency range over which the addition of *L* makes it closer to -90° than in the case of the RNC shunt.

It is evident from Figure 5 that the frequency range where the introduction of *L* allows to improve both the trend of the magnitude and phase of K_t depends on the value of *L*. The lower its value is, the wider the frequency range on which the trend of K_t improves is, and the lower the amount of improvement is (see Figure 5). This can be seen also looking at Figure 6a which shows the ratio between the K_t amplitude when *L* is employed over the amplitude of the RNC shunt. As an example, for *L*=1.43 H, the amplitude of the LRNC is improved compared to the RNC on a frequency range from about 1 Hz to a frequency value higher than 10 kHz. If the value *L*=14.33 H is considered, the amplitude increases from 1 Hz to about 285 Hz. However, the improvement of the amplitude is larger in the latter case.

Considering the phase, that of the LRNC with *L*=1.43 H is closer to -90° than that of the RNC up to about 190 Hz. Conversely, for the LRNC shunt with *L*=14.33 H, the phase is closer to -90° than that of the RNC up to about 110 Hz. This can be seen also looking at Figure 6b which shows the distance (in absolute value) of the K_t phase from the -90°. In this latter figure, the curves related to *L*=1.43 and 14.33 H are below the curve of the RNC shunt (red thin solid curve) up to about 190 and 110 Hz, respectively.

Therefore, the use *L*=14.33 H is expected to give a higher improvement in terms of attenuation (e.g. higher K_t magnitude) with respect to that achievable with the addition of an inductance of 1.43 H, but in a narrower frequency range.

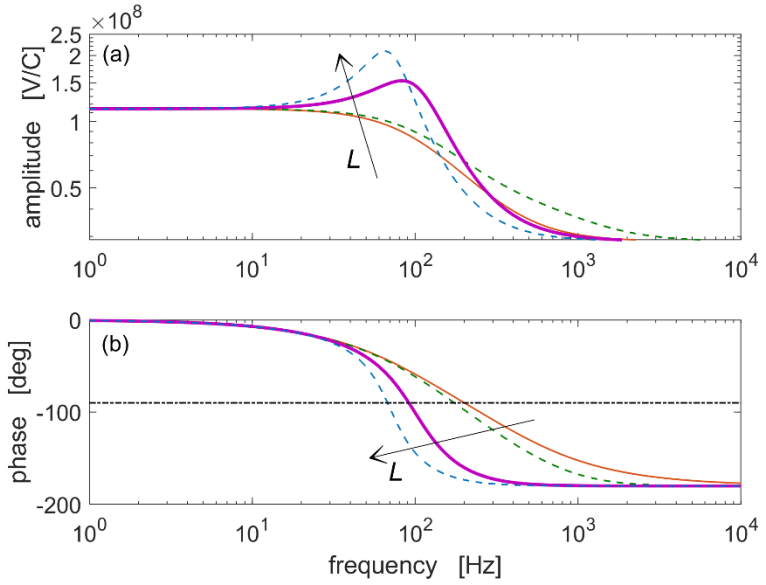

Figure 5: FRF of K_t for an RNC impedance (red solid thin curve) and for LRNC impedances with increasing values of *L* (type 1 shunt): amplitude (a) and phase (b). The mechanical system to be controlled is assumed to be a single-degree-of-freedom system with k_i=0.1, ω_i=2π·100 rad/s, C_∞=35 nF. The value of the NC was -43.75 nF. The used *L* values were 0, 1.43, 14.33, and 28.66 H. The black dash-dotted horizontal line in plot (b) indicates the phase value of -90°.

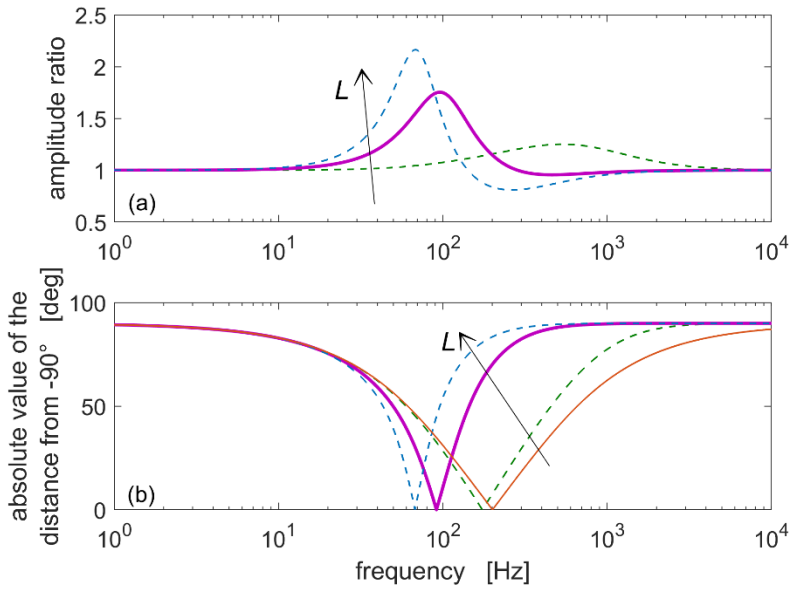

Figure 6: Ratio between the K_t amplitude when L is employed and the K_t amplitude of the RNC shunt (L values equal to 1.43, 14.33, and 28.66 H) (a) and distance (in absolute value) of the K_t phase from the -90° (L values equal to 0, 1.43, 14.33, and 28.66 H) (b). The mechanical system to be controlled is the same of Figure 5.

Through the analysis of the K_t FRFs, the presented example allows to evidence that the introduction of the electrical eigenfrequency generated by the addition of the inductance (Thomas et al., 2012) (named here as ω_e, see Table 2) is able to improve the control performance of the RNC shunt on a given frequency range thanks to a tuning of *L* and *R* different from that used in the case of traditional LR shunt. Indeed, it is recalled that here *L* is not used to build an optimised resonant shunt but to boost the performance of the resistive shunt coupled to an NC in a given frequency range.

The previous discussion has been based on the analysis of the controller FRF since it has allowed to clearly evidence the effect of the introduction of different *L* values in the shunt circuit. Therefore, the possible benefits provided by this configuration have been shown looking at the K_t characteristics. However, it is useful to look at these aspects also in terms of the achieved attenuation performance. To this purpose, Figure 7 shows, as an example, the attenuation and the attenuation improvement on a mode at frequency equal to ω_i with respect to the RNC shunt provided by the use of different values of *L* (and thus of ω_e) (positive numbers for the improvement plots mean an increase of the attenuation). In this case, the RNC shunt used as reference for the comparison is tuned for maximising the attenuation on a mode at approximately 1650 Hz. The attenuation is calculated (in decibel) as the ratio between the amplitude peak of the FRF (displacement/force) with the piezoelectric actuator short-circuited and the amplitude peak of the controlled FRF (displacement/force). Both for the LRNC and RNC shunt, the elements of the shunt impedance are connected in series (see Figure 4a). The curves of the figure allow to see the amount of attenuation and improvement achieved on the additional mode at ω_i for different values of *L*. This enables to show that the use of *L* provides an increase of attenuation on given frequency ranges. The higher *L* is, the narrower the frequency band of the improvement is (see Figure 7b, d and f). It is also evident that the maximum value of *L*, among those used in the figure, which is acceptable in this example is that equal to 0.15 H (see the thick curves in the figure). Indeed, up to this *L* value, the attenuation at the mode at 1650 Hz (i.e. that on which the RNC shunt is initially tuned) increases, while with the highest *L* value employed (i.e. 0.2 H) the attenuation on this mode worsens.

A significant outcome of the figure is also that, for the system considered, the maxima improvements provided by the introduction of the inductance are not so different with different damping values. This is particularly important when the damping value is high (e.g. 1%) and thus the overall attenuation is not high. It is also noticed that, since the results shown in Figure 7 were obtained using a single-degree-of-freedom approximation around the mode at ω_i (see Section 2.1), the results shown are approximated when ω_i is close to 1650 Hz (i.e. when ω_i approaches the mode on which the RNC shunt was initially tuned) because of modal superimposition.

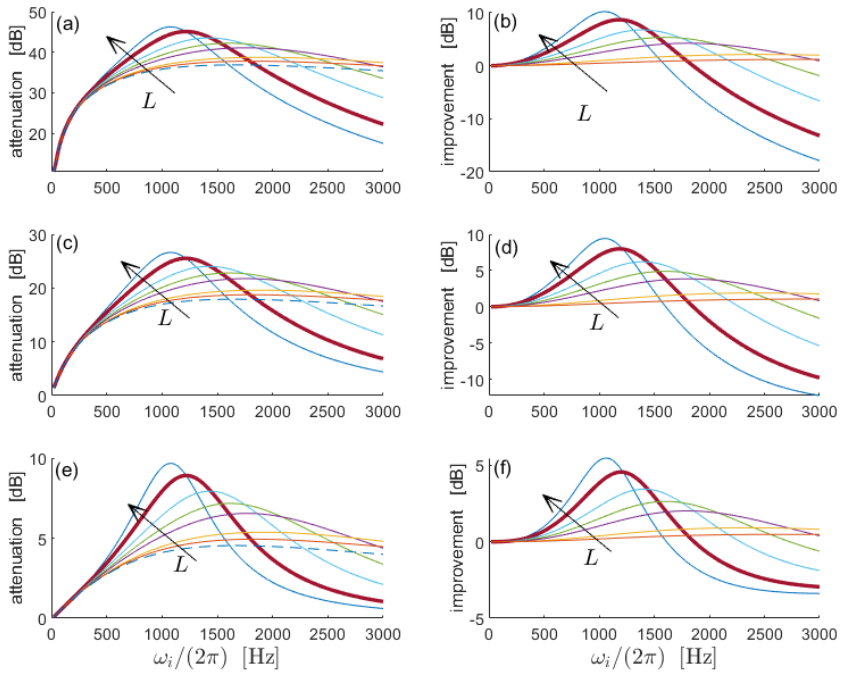

Figure 7: Attenuation and attenuation improvement compared to the RNC shunt as functions of ω_i for different L values (i.e. 0, 0.01, 0.02, 0.05, 0.07, 0.1, 0.15 and 0.2 H) (type 1 shunt in Figure 4). The mechanical system to be controlled is assumed to be a single-degree-of-freedom system with k_i=0.1, C_{pi}=35 nF and ξ_i=0.01% (a and b), ξ_i=0.1% (c and d) and ξ_i=1% (e and f). The value of R was set to 1000 Ω, which is the optimal value of R, R^{opt}, for a mode at approximately 1650 Hz (Berardengo et al., 2016c). The dashed curves are related to the use of an RNC impedance (i.e. L=0 H), while the thick curves are related to L=0.15 H. $-C \cong -1.57C_{pi}$

As mentioned, the three elements R, L and the NC -C are connected in series in the previous example. However, four layouts are possible, as shown in Figure 4 and thus the behaviour of K_t for all the four possible layouts was analysed. The expression of K_t for all the four types of impedances is provided in Table 4. This analysis showed that types 1 and 3 provide an improvement of the control action at low frequency (e.g. Figure 5 and Figure 7), while Types 2 and 4 improve the attenuation at high frequency. This point will be treated in more detail in the next subsection.

From here on, the analysis will be focused on problems involving low frequency modes and, in particular, type 1 impedance will be considered. Nevertheless, analyses similar to those reported here for type 1 can be easily carried out for the other three circuit types and some results will be presented in in the next subsection.

Table 4: Expression of $K_t(s)$ for the four types of shunt circuits

Circuit Type	Expression of $K_t(s)$
1	$\frac{LCs^2 + RCs - 1}{-C - C_\infty(LCs^2 + RCs - 1)}$
2	$\frac{-LRCs^2 + Ls + R}{LRCC_\infty s^2 + Ls(C - C_\infty) + R(C - C_\infty)}$
3	$\frac{s(Ls + R)}{Ls^2(C - C_\infty) + Rs(C - C_\infty) - 1}$
4	$\frac{LRs^2}{LRs^2(C - C_\infty) - Ls - R}$

3.2 General rules for the inductance tuning

So far, the effect of the value of *L* has been analysed mainly looking at the trend of K_t (e.g. see Figure 5) and showing that, for type 1 shunt, the higher the value of *L* is, the narrower the frequency band where the attenuation improvement occurs is. The analysis presented in this section highlights some common behaviours shown by different types of systems when *L* is added in the shunt. This will lead to define general rules for tuning the value of *L*.

Figure 8 shows the attenuation improvement given by the LRNC shunt compared to the RNC shunt for a mode at ω_i as a function of the ratios ω_e/ω_r (and, thus, as a function of *L*, see Table 2) and ω_i/ω_r, where ω_r is the eigenfrequency value at which the control action of the RNC shunt is initially maximised. It is recalled that, to maximise the effect of the RNC shunt at a frequency ω_r, the value of *R* must be set according to the system characteristics and the NC value (Berardengo et al., 2016c):

$$R^{\text{opt}} = \frac{\sqrt{2}}{C_{\text{eq}}\omega_r\sqrt{\tilde{k}_r^2 + 2}} \tag{10}$$

where the expressions of C_{eq} and $\tilde{k}_r$ are given in Table 2 .The results of the analysis were obtained using the single-degree-of-freedom model presented in the subsection named 'FRF of the EMS and stability' and, thus, under the hypothesis of low modal density. Therefore, the presented results have to be considered as approximate when ω_i/ω_r is close to 1 (i.e. in case the i^{th} mode is very close to the r^{th}).

The various plots of Figure 8 are related to different systems chosen as examples and can be considered of general validity since are almost not dependent on the value of ω_r. Looking at Figure 8, it is possible to clearly identify two areas: the first, in the top-left part of each of the plots, where the LRNC shunt allows to improve the attenuation at the mode at ω_i (i.e. positive numbers on the iso-lines), and another, in the bottom-right part, where the performance is worsened. This behaviour evidences that, as mentioned, the chosen layout (Type 1, see Figure 4a) is fine for acting mainly at frequencies lower than ω_r, while its effect at higher frequencies is quite limited. The two areas of the plot are separated by the iso-line associated to the 0 dB value. Therefore, this line can be considered as the reference for the tuning of the inductance in order to improve the attenuation in a given frequency band. It must be evidenced that the effect of the damping value ξ_i is just to change the value of the attenuation improvement, leaving almost unchanged the trend of the plot (compare Figure 8a and Figure 8b). The same applies when changing the value of k_i (compare Figure 8a and Figure 8c) and $\tilde{k}_i$ (the value of $\tilde{k}_i$ changes when the value of the NC is changed, see Table 2) (compare Figure 8a and Figure 8d). Hence, the curve related to 0 dB is always approximately in the

same area of the whole plot, regardless the characteristics of the system considered. A rough estimation of the 0 dB iso-curve can be, thus, derived (see the red dashed lines in Figure 8):

$$\frac{\omega_{\mathrm{e}}}{\omega_r} = 0.719\frac{\omega_i}{\omega_r} + 0.005 \tag{11}$$

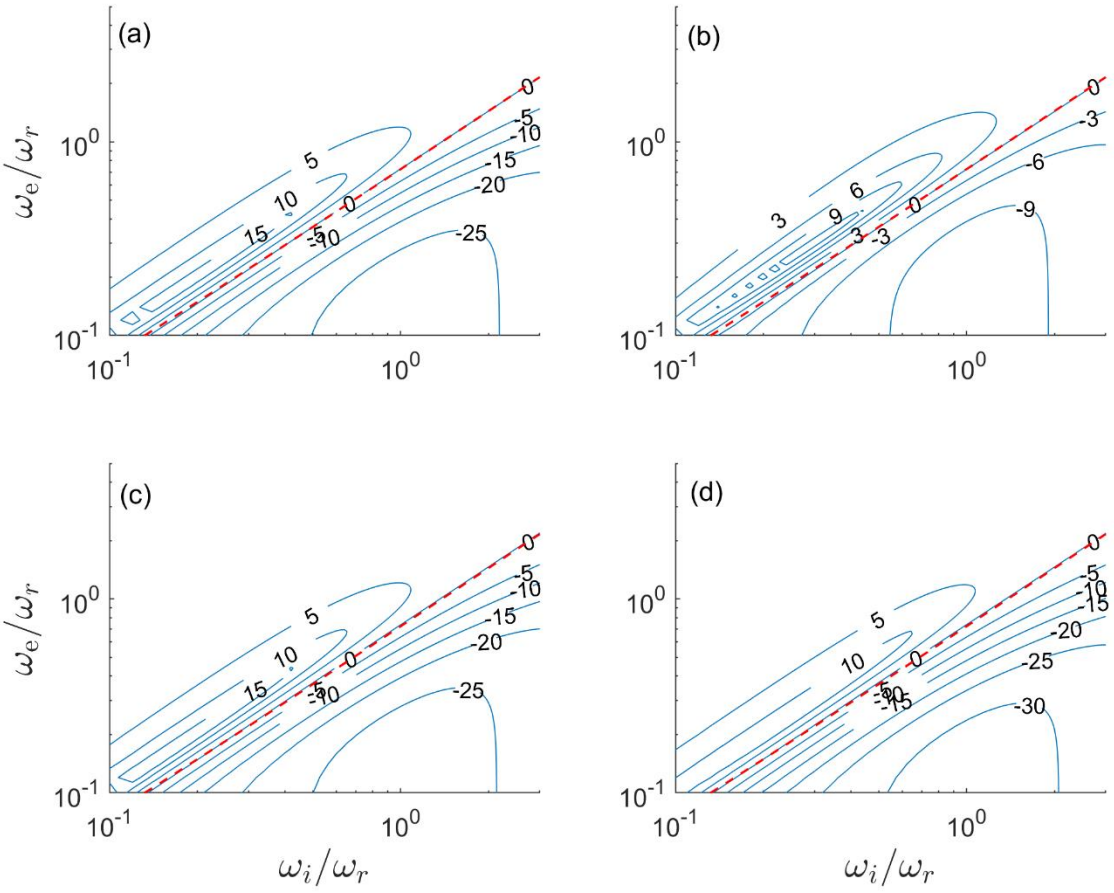

Figure 8: Iso-lines (solid blue lines) showing the attenuation improvement (in decibel) due to the addition of L to the RNC shunt (type 1 circuit) for a mode with eigenfrequency ω_i as a function of ω_i/ω_r and $\omega_{\mathrm{e}}/\omega_r$. ξ_i=10^{-3}, k_i=0.1 and $\tilde{k}_i$=0.3 (a), ξ_i=10^{-2}, k_i=0.1 and $\tilde{k}_i$=0.3 (b), ξ_i=10^{-3}, k_i=0.2 and $\tilde{k}_i$=0.3 (c), ξ_i=10^{-3}, k_i=0.1 and $\tilde{k}_i$=0.4 (d). The capacitance value used to calculate C_{eq} and then ω_{e} (see Table 2) is that of mode r ($C_{\mathrm{p}i}$ and $C_{\mathrm{p}r}$ are assumed so close that $C_{\mathrm{p}i} = C_{\mathrm{p}r}$). The dashed red lines show the approximated trend of the 0 dB iso-line given in Eq. (11).

Numerical simulations were carried out on systems with non-dimensional damping ratio ξ_i between 0.01% and 6% and with k_i from 0.025 to 0.3 to test the effectiveness of Eq. (11) in approximating the 0 dB improvement iso-line. These boundary values were chosen as representative of the most common situations that can be found in practical applications. In all these cases, Eq. (11) was found in good agreement with the actual system behaviour, as shown in Figure 8 for some systems chosen as examples (see the red dashed lines in good agreement with the 0 dB improvement iso-lines).

Even if it is not possible to have a general rule for setting the value of L in order to achieve a given amount of attenuation improvement in a given frequency range, it is possible to use Eq. (11) to set its value in order to assure attenuation improvement on the frequency range of interest. Indeed, if $\omega_{\mathrm{e}}/\omega_r$ is set such that an attenuation improvement equal to 0 dB (i.e. no change of the attenuation consequent to the introduction of L in the shunt impedance) is achieved at the maximum eigenfrequency of interest, all the modes at lower frequencies will undergo an attenuation improvement, whereas modes at higher frequencies will be

amplified compared to the RNC shunt. Furthermore, Eq. (11) evidences that, usually, for a given value of ω_e, the maximum value of ω_i for which an attenuation improvement is achieved is slightly higher than ω_e. This behaviour can also be grasped thinking at the relative position of the electrical and mechanical eigenfrequencies: the closer they are, the higher the achievable improvement is. Moreover, a worsening of the attenuation is expected if ω_e is set to a value rather lower than ω_i.

In practice, when a given number of modes must be controlled with type 1 circuit in a given frequency range, the following procedure can be employed:

1. Set the value of the NC and the resistance *R* according to the usual criteria discussed in the literature (e.g. Eq. (10) or (Berardengo et al., 2016c)) in order to have vibration attenuation on the desired mode or frequency range.
2. Add *L* in the shunt. Its value (and, thus, that of ω_e) can be chosen looking at the 0 dB curve in Figure 8 (or using Eq. (11)), in order to improve (or at least maintain unchanged) the attenuation on the interesting modes. According to Eq. (11) and Figure 8, in case ω_r is the highest mode in frequency to be attenuated, then ω_e/ω_r can be set equal to approximately 0.72 (i.e. $\omega_e/\omega_r = 0.719 \times 1 + 0.005$). This allows to maximise the attenuation improvement on the lower modes, maintaining the attenuation unchanged for the mode at ω_r. If, instead, the attenuation on ω_r must be increased by adding *L*, the value of ω_e/ω_r must be set higher than 0.72 (i.e. increasing the value of ω_e). When the maximum ω_i to be controlled (named $\omega_i^{\max}$) is higher than ω_r, the value of ω_e/ω_r can be derived using Eq. (11) and posing $\omega_e/\omega_r = (\omega_i^{\max}/\omega_r) \times 0.719 + 0.005$. This equation allows to determine the minimum value of ω_e/ω_r to be used with the aim of not worsening the attenuation on the interesting modes. Then, Figure 8 can indicate the amount of improvement expected for the considered modes. As general notation, it is possible to suggest to use type 1 circuit with $\omega_i^{\max}$ equal or slightly higher than ω_r because, when it is largely higher than ω_r, the amount of improvement which can be achieved on the lower modes is limited (i.e. ω_e/ω_r must be increased a lot over the 0 dB iso-line, see Figure 8).
3. Once the value of ω_e has been chosen, the value of *L* can be calculated with the expression linking ω_e and *L* in Table 2 (using the value of C_{pi} of the mode at $\omega_i^{\max}$ in the expression of C_{eq}).
4. In case a map like those of Figure 8 are needed for a more a detailed description of the attenuation improvement on all the interesting modes, numerical simulations can be carried out with the previously presented model. This can also help for a more refined choice of the inductance value.

Finally, if the focus is on modes higher than ω_r, it would be better to consider different layouts for the shunt circuit such as types 2 or 4 (see Figure 4).

A specific case can be now treated in detail and it is related to the description of the attenuation improvement for the mode at ω_r (thus, for the mode to which the RNC shunt was specifically tuned) and this is depicted in Figure 9. Figure 9a and Figure 9b show that the attenuation improvement on the mode at ω_r has always the same shape, regardless the values of the EMS parameters. The parameter most influencing the value of the improvement is the distance between ω_r and ω_e. An interesting fact is that around ω_e/ω_r=1 the slope of the curve changes gradually and the curve peak is smooth. The main reason is that the value of *R* used is that for RNC shunt, which is often significantly higher than the optimal resistance values used in resonant shunt (Thomas et al., 2012). This allows to have a good robustness of the control because even a change of some system or impedance parameters does not change significantly the control performance. Moreover, it can be noticed that an improvement of the control performance on the mode at ω_r is always achieved when ω_e is higher than approximately $0.72\omega_r$ as shown also by Eq. (11).

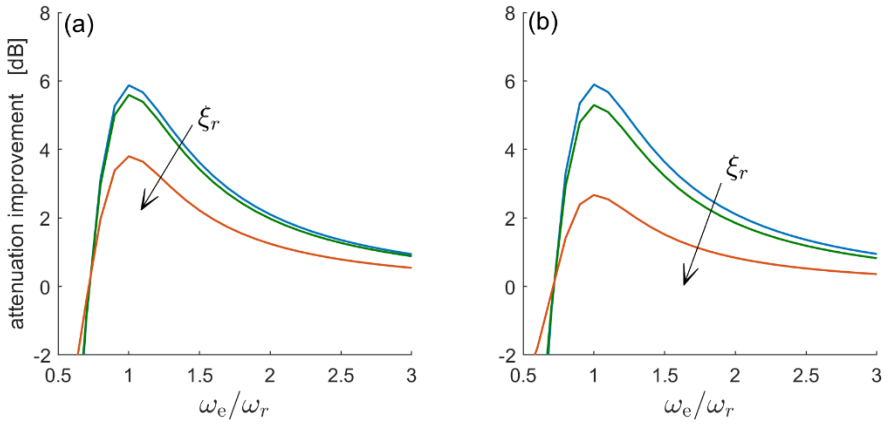

Figure 9: Improvement of the attenuation on mode r for different ξ_r values (i.e. 0.01%, 0.1% and 1%) and two different systems: $k_r = 0.1$ and $-C = -1.25C_{pr}$ (a), and $k_r = 0.1$ and $-C = -1.80C_{pr}$ (b). $\omega_r = 2\pi \times 100$ rad/s. Type 1 shunt circuit.

Figure 10 instead shows plots similar to those of Figure 8 but for circuits 2 and 4. As mentioned, these circuits are able to improve the attenuation performance at frequencies above (or slightly below) ω_r. Considering type 4 circuit, the 0 dB iso-line can be roughly derived as (see the red dashed line in Figure 10b):

$$\frac{\omega_e}{\omega_r} = 1.36\frac{\omega_i}{\omega_r} + 0.012 \tag{12}$$

This equation allows to apply a procedure similar to that given for type 1 circuit here above. The only difference is that circuit types 1 and 3 are fruitfully used to improve the attenuation of modes lower (in frequency) or slightly higher than ω_r, while circuit types 2 and 4 are fruitfully employed to improve the attenuation of modes higher or slightly lower than ω_r.

Finally, it is worth noticing that equations similar to Eqs. (11) and (12) can be derived also for circuit types 2 and 3.

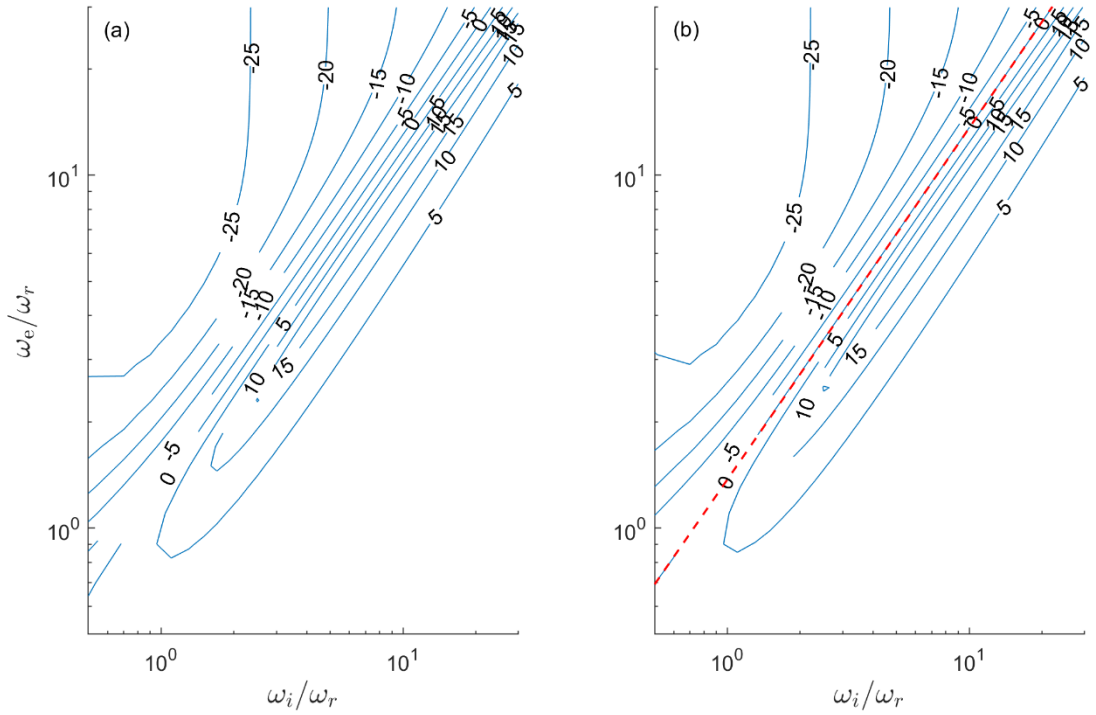

Figure 10: Iso-lines (solid blue lines) showing the attenuation improvement (in decibel) due to the addition of L to the RNC shunt for a mode with eigenfrequency ω_i as a function of ω_i/ω_r and ω_e/ω_r for a system with ξ_i=10^{-3}, k_i=0.1 and $\tilde{k}_i$=0.3: type 2 circuit (a), type 4 circuit (b). The capacitance value used to calculate C_{eq} and then ω_e (see Table 2) is that of mode r (C_{pi} and C_{pr} are assumed so close that $C_{pi} = C_{pr}$). The dashed red line in plot (b) shows the approximated trend of the 0 dB iso-line given in Eq. (12).

3.3 Benefits of the new circuit for a multi-degree-of-freedom system: example with three modes

This subsection aims at showing the beneficial effect of the properly tuned inductance on a multi-degree-of-freedom system. To this purpose, a realistic EMS with three modes is employed as an example and the attenuation improvements achievable with an LRNC shunt (type 1) are quantitatively discussed.

The modal data of the system chosen as an example are gathered in Table 5. At first, the value of R is chosen to be the optimal one for the third mode, which is the highest in this case (thus, $\omega_i^{\max}/\omega_r$=1). Following the tuning procedure presented previously, the value of ω_e/ω_r should be set equal to approximately 0.72 (see Eq. (11)) in order to improve the attenuation on the modes lower than the highest among the interesting ones (i.e. the third in this case) and without deteriorating the attenuation on the highest mode. In this case, this leads to an inductance value of about 0.2 H.

In order to present the achieved attenuation improvement, Figure 11a and Figure 11b show the attenuation and the attenuation improvement with respect to the RNC shunt, respectively, for all the three modes as functions of the L value. From these figures, it is possible to notice that this setting enables to improve the attenuation on the first and second modes of about 5.5 dB, without deteriorating the attenuation on the third, as expected.

However, as mentioned and shown in Figure 8, in case also the performance on the highest mode of interest has to be improved, the value of ω_e/ω_r should be set slightly higher than 0.72. Indeed, looking at Figure 11b, it can be noticed that a value of L equal to approximately 0.14 H leads to an attenuation

improvement equal or higher than 4 dB on all the modes (see the vertical dashed line in Figure 11b). This inductance value corresponds to $\omega_e/\omega_r = 0.866$, thus higher than 0.72, and to $\omega_e/(2\pi) \cong$690 Hz.

Table 5: Modal data of a system with three modes

Mode number	$\omega_i/2\pi$ [Hz]	ξ_i [%]	k_i	C_{pi} [nF]
1	400	0.1	0.03	35.05
2	600	0.1	0.02	35.03
3	800	0.1	0.03	35.00

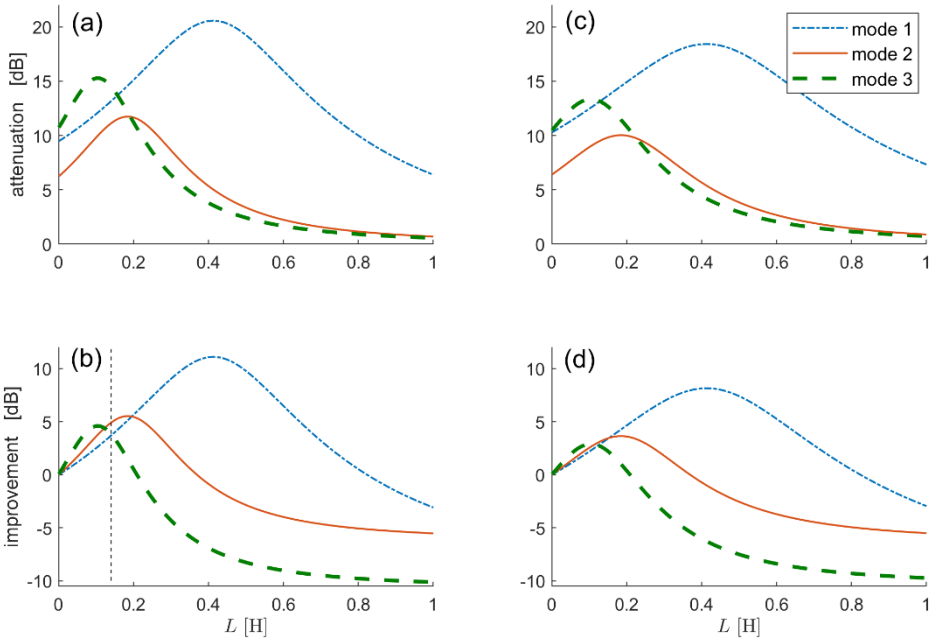

Figure 11: Attenuation on the modes of Table 5 as function of the value of *L* (type 1 shunt) (plots a and c) and the corresponding attenuation improvement compared to the case of using an RNC shunt (plots b and d). Here, *-C*=-38.585 nF. The value of *R* is the optimal one for the third mode (plots a and b) and for the second mode (plots c and d).

Figure 11c and Figure 11d show the attenuation and attenuation improvement, respectively, when *R* is the optimal one for the second mode. Therefore, since the maximum eigenfrequency of interest is the third, $\omega_i^{\max}/\omega_r$ is equal to 1.33. In this case, the addition of the inductance does not have to deteriorate the performance on the third mode. Therefore, setting ω_e/ω_r =0.96 using Eq. (11) (and thus *L* equal to approximately 0.2 H) leads to an improvement of about 3.5 and 5 dB on the first and second mode, respectively. It is evident that the amount of improvement decreases with respect to the previous case for a given value of *L* (compare Figure 11b and Figure 11d). This is in accordance with Figure 8. However, as in the previous case, a higher value of ω_e/ω_r would be needed to improve the attenuation of all the modes and, in turn, this would imply a lower improvement on the first two. For example, using a value of *L* of approximately 0.12 H (ω_e/ω_r of about 1.25), it is possible to improve the attenuation of 2.8 dB on modes 1 and 3 and of 3 dB on mode 2.

4 Experimental tests

The set-up used for showing experimentally the benefits provided by the addiction of *L* to an RNC shunt is a cantilever beam in aluminium with a piezoelectric patch bonded at the clamped end. The beam was 161 mm long, 25 mm wide and 1 mm thick, while the piezoelectric patch was 50 mm long, 25 mm wide and 0.4 mm thick.

The structure was excited by means of a contactless actuator constituted by a coil and a magnet bonded to the beam close to its tip. Making current flowing in the coil allows to exert a force to the beam and such a force was proportional to the current flowing in the coil (Thomas et al., 2003). This current was measured by means of a current clamp, while the response of the structure was measured through a laser Doppler velocimeter. The disturbance provided to the beam was of random nature, exciting the first four bending modes. For further details on the experimental set-up, see (Berardengo et al., 2017a).

It is worth mentioning that this set-up was chosen for the tests because it shows modes which are widely spaced in frequency (which is a disadvantageous situation for this approach; see previously) and thus it is a good test-case to show the effectiveness of this method.

Several tests were carried out employing different circuit layouts (see Figure 4). Here, only the tests related to types 1 and 2 are shown for the sake of conciseness, and also because the behaviour of type 1 and 2 circuits is similar to that of type 3 and 4, respectively. Particularly, to highlight the outcomes of the paper, two tests are shown for type 1 layout (named tests 1 and 2 in Table 6). In the two tests, the RNC shunt was tuned on two different modes of the system. The test referred to as test 3 in Table 6 is instead related to the use of type 2 circuit.

The NC employed in these tests was built with an operational amplifier OPA445 using the layout in Figure 12. More details about this architecture can be found in (Berardengo et al., 2016c).

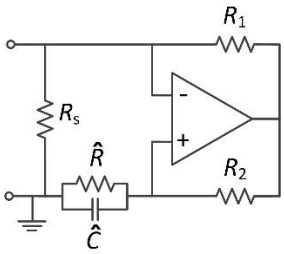

Figure 12: Layout of the NC used in the experiments.

Table 6: Data of the tests

Parameter	Test 1	Test 2	Test 3
$\omega_1\ /2\pi$ [Hz]	32.55	32.60	32.61
C_{p1} [nF]	50.18	50.18	50.18
ξ_1 [%]	0.47	0.41	0.43
k_1	0.15	0.15	0.15
$\omega_2\ /2\pi$ [Hz]	194.56	194.45	194.50
C_{p2} [nF]	49.35	49.35	49.35
ξ_2 [%]	0.38	0.37	0.38
k_2	0.04	0.04	0.04
$\omega_3\ /2\pi$ [Hz]	504.10	503.06	503.65
C_{p3} [nF]	49.23	49.23	49.23
ξ_3 [%]	0.33	0.31	0.32
k_3	0.04	0.04	0.04
$\omega_4\ /2\pi$ [Hz]	1001.24	999.81	1000.99
C_{p4} [nF]	48.38	48.38	48.38
ξ_4 [%]	0.44	0.42	0.46
k_4	0.10	0.10	0.10
$\hat{R}$ [MΩ]	0.610	0.610	0.610
$\hat{C}$ [nF]	68.50	68.50	68.50
R_1 [kΩ]	14.335	13.089	13.089
R_2 [kΩ]	11.500	11.500	11.500
R_s [MΩ]	0.78	0.71	0.71
C [nF]	54.95	60.19	60.19
Shunt resistance tuned on mode	3	4	3
R [kΩ]	0.674	0.651	1.175
$\omega_{\mathrm{e}}/\omega_r$	from 0.89 to 2.03	from 0.70 to 1.01	from 0.82 to 1.42

5.1 Tests with Type 1 circuit

The results of tests 1 and 2 with a series NC and an LR in series (i.e. type 1 circuit) are shown in Figure 13a and Figure 13b, respectively. These figures show the attenuation improvement as a function of the value of *L* when *R* is tuned on the third and fourth mode, respectively. When the inductance is added in the shunt, the corresponding values of $\omega_{\mathrm{e}}/\omega_r$ are provided in the last row of Table 6. The curves are obtained by means of numerical simulations while the markers are the experimental results. These attenuation improvements are derived from the obtained FRFs (displacement/force). As an example, Figure 14 shows the experimental and numerical FRFs (the numerical FRFs have been derived by means of the model presented in the section named 'Model of the EMS') for test 2 in Table 6 in the cases of piezoelectric patch short-circuited, shunted with the RNC impedance, and with the LRNC shunt with two different values of *L*. The experimental FRFs show to be in satisfactory agreement with the numerical FRFs.

The first mode is not shown in the plots of Figure 13 because the trend of the improvement as a function of *L* is flat both in simulations and experiments, in accordance with the results of Figure 8 (i.e. this mode is too far from ω_r to experience a significant attenuation improvement). The agreement between the

experimental results and the simulations is good and this means that the model is able to properly predict the attenuation change when adding *L* in the shunt circuit.

In both tests 1 and 2, modes 1 and 2 show low or negligible improvements because they are very far in frequency from modes 3 and 4. Therefore, the additional *L* has no effect in that frequency range. Considering the other modes, in test 1, the ω_e/ω_r value has to be set higher than 1.43 in order to have an attenuation improvement on all the modes (i.e. third and fourth). From Figure 13a, it can be seen that a value of *L* of approximately 78 mH (which corresponds to $\omega_e/\omega_r = 1.78$) leads to an attenuation improvement of about 2 dB on both mode 3 and 4. Considering test 2, to improve the attenuation also on mode four (i.e. that on which the *R* is tuned and which is also the highest mode of interest), the ω_e/ω_r has to be set higher than 0.72 (see Eq. (11)). In this case, Figure 13b shows that a value of *L* of about 150 mH, which corresponds to ω_e/ω_r=0.83, leads to an attenuation improvement of about 3 dB on both mode 3 and 4.

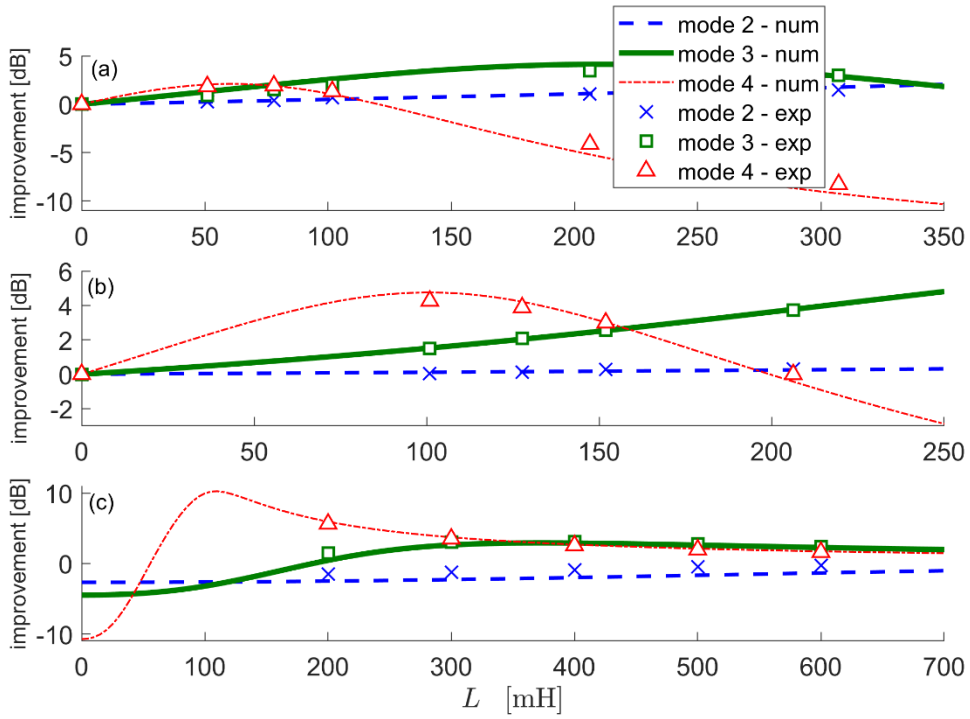

Figure 13: Improvement of the attenuation as a function of the value of *L* for three modes in test 1 (shunt type 1) (a), test 2 (shunt type 1) (b) and test 3 (shunt type 2) (c).

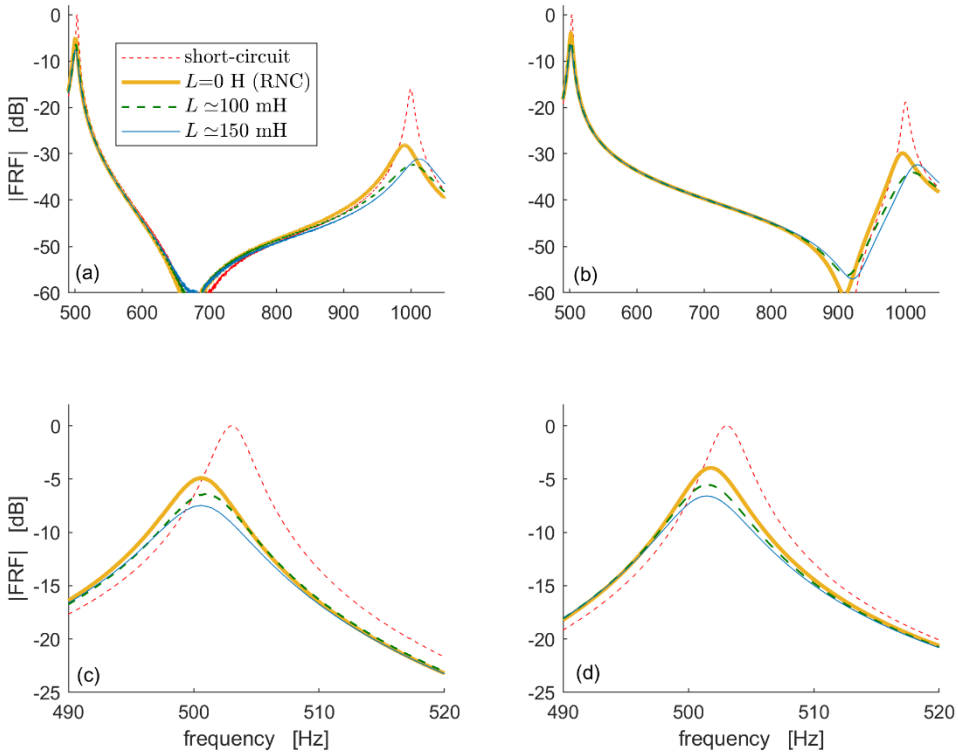

Figure 14: Experimental (a) and numerical (b) FRFs (displacement over force) for test 2 of Table 6 zoomed on modes 3 and 4. The curves in short-circuit have been scaled to have peaks at 0 dB at the third eigenfrequency for an easy quantitative comparison of the curves. Plots (c) and (d) show the curves of plots (a) and (b), respectively, zoomed on mode 3.

Other tests were carried out, which showed similar results. Therefore, they are not shown here for the sake of conciseness. It is noticed that the values of L were small enough to be built by means of coils.

Finally, Table 7 reports the experimental attenuation values obtained when using the RNC shunt (thus, without the addition of L in the shunt circuit) for modes 2 to 4. These data, together with those plotted in Figure 13a and Figure 13b, allow to calculate the overall attenuation achievable adding L in the shunt circuit.

Table 7: Experimental vibration attenuation values with the RNC shunt

	Test 1	Test 2
Attenuation for mode 2 [dB]	5.32	3.13
Attenuation for mode 3 [dB]	7.42	4.91
Attenuation for mode 4 [dB]	14.39	12.06

5.2 Tests with Type 2 circuit

In this case, type 2 circuit, with the inductance in parallel to the resistance, is used, with an NC in series (see Figure 4b).

Figure 13c shows the attenuation improvement as function of the value of *L* with *R* tuned on the third mode. When the inductance is added in the shunt, the corresponding values of ω_e/ω_r are provided in the last row of Table 6. This time the inductance was built by using a network of operational amplifiers (Beck et al., 2013; Seba et al., 2006; Thomas et al., 2012). The agreement between the curves yielded numerically and the experiments is good.

The expected behaviour of this layout is to improve the attenuation level at frequencies higher or slightly lower than ω_r. Indeed, setting $\omega_e/\omega_r \cong 1.36$ would lead to 0 dB improvement on the third mode, to an improvement on higher modes and to a worsening of the attenuation level on lower modes (see Eq. (12), as an approximation for type 2 circuit). In order to achieve an improvement of the vibration attenuation also on the third mode, values of ω_e/ω_r lower than 1.36 have to be employed (see Figure 10). Indeed, Figure 13c shows that setting $\omega_e/\omega_r \cong 1$, which corresponds to a value of *L* of about 370 mH, leads to an attenuation improvement of about 3 dB on both mode 3 and 4. Conversely, modes 2 and 1 show a worsening of the attenuation. Therefore, the experiments confirm that Type 2 circuit focuses the action of the inductance on a frequency band higher than ω_r.

Also in this case, other tests were carried out, leading to similar results and they are not shown here for the sake of conciseness.

6 Conclusion

This paper has dealt with piezoelectric shunt damping. An approach for enhancing, in a given frequency range, the attenuation performance provided by resistive impedances coupled to negative capacitances is proposed. It consists in the addition of an inductance to the shunt circuit, leading to the addition of a resonance to the whole system. The LR shunt is not used for single-mode control as usual, but to increase the broadband control capability of the resistive shunt. This is accomplished by a different tuning of the electrical components.

The reason why the addition of the inductance provides benefits is explained by showing the feed-back nature of the shunt damping. Among the different possible shunt impedance layouts proposed, some of them are found to be effective at low frequency, while others must be preferred when the control has to be improved at high frequency. For all of them, practical rules for the tuning of the inductance value can be derived.

The advantages of this approach were evidenced with some numerical examples. Then, the technique was validated by means of experimental tests.

ACKNOWLEDGMENTS

This research has financially been supported at University of Parma by the Programme "FIL-Quota Incentivante" of University of Parma and co-sponsored by Fondazione Cariparma. Furthermore, the Italian Ministry of Education, University and Research is acknowledged by the staff of Politecnico di Milano for the support provided through the Project "Department of Excellence LIS4.0 - Lightweight and Smart Structures for Industry 4.0".

DECLARATION OF CONFLICTING INTERESTS

The author(s) declared no potential conflicts of interest with respect to the research, authorship, and/or publication of this article.

References

Andreaus, U., Porfiri, M., 2007. Effect of Electrical Uncertainties on Resonant Piezoelectric Shunting. Journal of intelligent material systems and structures 18, 477–485.

Beck, B.S., Cunefare, K.A., Collet, M., 2013. Response-based tuning of a negative capacitance shunt for vibration control. Journal of Intelligent Material Systems and Structures 25, 1585–1595.

Behrens, S., Fleming, A.. J., Moheimani, S.O.R., 2003a. A broadband controller for shunt piezoelectric damping of structural vibration. Smart materials and Structures 18, 18–28.

Behrens, S., Moheimani, S.O.R., Fleming, a. J., 2003b. Multiple mode current flowing passive piezoelectric shunt controller. Journal of Sound and Vibration 266, 929–942.

Berardengo, M., Bonsignori, R., Cigada, A., Manzoni, S., 2016a. Enhanced vibration damping by means of a negative capacitance. In: Conference Proceedings of the Society for Experimental Mechanics - XXXIV International Modal Analysis Conference (IMAC), Orlando (USA), 25-28 January 2016, ISBN: 9783319299556, Vol. 7. pp. 75–81.

Berardengo, M., Cigada, A., Manzoni, S., Vanali, M., 2015a. Vibration Control by Means of Piezoelectric Actuators Shunted with LR Impedances: Performance and Robustness Analysis. Shock and Vibration 2015, ID 704265.

Berardengo, M., Manzoni, S., Conti, A.M., 2017a. Multi-mode passive piezoelectric shunt damping by means of matrix inequalities. Journal of Sound and Vibration 405, 287–305.

Berardengo, M., Manzoni, S., Thomas, O., Giraud-Audine, C., 2015b. A new electrical circuit with negative capacitances to enhance resistive shunt damping. In: ASME 2015 Conference on Smart Materials, Adaptive Structures and Intelligent Systems, SMASIS 2015.

Berardengo, M., Manzoni, S., Thomas, O., Vanali, M., 2018. Piezoelectric resonant shunt enhancement by negative capacitances: optimisation, performance and resonance cancellation. Journal of Intelligent Material Systems and Structures 29, 2581–2606.

Berardengo, M., Manzoni, S., Vanali, M., 2016b. The Behaviour of Mistuned Piezoelectric Shunt Systems and Its Estimation. Shock and Vibration 2016, 9739217.

Berardengo, M., Thomas, O., Giraud-Audine, C., Manzoni, S., 2016c. Improved resistive shunt by means of negative capacitance: new circuit, performances and multi-mode control. Smart Materials and Structures 25, 075033.

Berardengo, M., Thomas, O., Giraud-Audine, C., Manzoni, S., 2017b. Improved shunt damping with two negative capacitances: An efficient alternative to resonant shunt. Journal of Intelligent Material Systems and Structures 28, 2222–2238.

Bricault, C., Pézerat, C., Collet, M., Pyskir, A., Perrard, P., Matten, G., Romero-García, V., 2019. Multimodal reduction of acoustic radiation of thin plates by using a single piezoelectric patch with a negative capacitance shunt. Applied Acoustics 145, 320–327.

Caruso, G., 2001. A critical analysis of electric shunt circuits employed in piezoelectric passive vibration damping. Smart Materials and Structures 10, 1059–1068.

Darleux, R., Lossouarn, B., Deü, J.F., 2020. Broadband vibration damping of non-periodic plates by piezoelectric coupling to their electrical analogues. Smart Materials and Structures 29, ID 054001.

de Marneffe, B., Preumont, a, 2008. Vibration damping with negative capacitance shunts: theory and experiment. Smart Materials and Structures 17, 035015.

Dell'Isola, F., Maurini, C., Porfiri, M., 2004. Passive damping of beam vibrations through distributed electric networks and piezoelectric transducers: Prototype design and experimental validation. Smart Materials and Structures 13, 299–308.

Ducarne, J., Thomas, O., Deü, J.-F., 2012. Placement and dimension optimization of shunted piezoelectric patches for vibration reduction. Journal of Sound and Vibration 331, 3286–3303.

Hagood, N., Flotow, A. von, 1991. Damping of structural vibrations with piezoelectric materials and passive electrical networks. Journal of Sound and Vibration 146, 243–268.

Heuss, O., Salloum, R., Mayer, D., Melz, T., 2016. Tuning of a Vibration Absorber with Shunted Piezoelectric Transducers. Archive of Applied Mechanics 86, 1715–1732.

Høgsberg, J., Krenk, S., 2015. Balanced calibration of resonant piezoelectric RL shunts with quasi-static background flexibility correction. Journal of Sound and Vibration 341, 16–30.

Hurwitz, A., 1895. On the conditions under which an equation has only roots with negative real parts. Mathematische Annalen 46, 273–284.

Lossouarn, B., Aucejo, M., Deü, J.F., Cunefare, K.A., 2018. Design of a passive electrical analogue for piezoelectric damping of a plate. Journal of Intelligent Material Systems and Structures 29, 1301–1314.

Matveenko, V.P., Iurlova, N.A., Oshmarin, D.A., Sevodina, N. V, Iurlov, M.A., Iurlova, N.A., Oshmarin, D.A., Sevodina, N. V, 2018. An approach to determination of shunt circuits parameters for damping vibrations. International Journal of Smart and Nano Materials 9, 135–149.

Moheimani, S., Fleming, A., 2006. Piezoelectric transducers for vibration control and damping. Springer, London.

Moheimani, S.O.R., Fleming, A.J., Behrens, S., 2003. On the feedback structure of wideband piezoelectric shunt damping systems. Smart Materials and Structures 12, 49–56.

Neubauer, M., Oleskiewicz, R., Popp, K., Krzyzynski, T., 2006. Optimization of damping and absorbing performance of shunted piezo elements utilizing negative capacitance. Journal of Sound and Vibration 298, 84–107.

Oshmarin, D., Iurlova, N., Sevodina, N., Iurlov, M., 2019. Algorithm for the layout of a piezoelectric element in an elastic medium providing the maximal piezoelectric effect within a specified frequency range. International Journal of Smart and Nano Materials 10, 268–284.

Park, C.H., Baz, A., 2005. Vibration Control of Beams with Negative Capacitive Shunting of Interdigital Electrode Piezoceramics. Journal of Vibration and Control 11, 331–346.

Park, C.H., Inman, D.J., 2003. Enhanced Piezoelectric Shunt Design. Shock and Vibration 10, 127–133.

Pohl, M., 2017. An adaptive negative capacitance circuit for enhanced performance and robustness of piezoelectric shunt damping. Journal of Intelligent Material Systems and Structures 28, 2633–2650.

Preumont, A., 2002. Vibration Control of Active Structures: An Introduction, 2nd ed. Kluwer Academic Publisher, Dordrecht.

Raze, G., Paknejad, A., Zhao, G., Collette, C., Kerschen, G., 2020. Multimodal vibration damping using a simplified current blocking shunt circuit. Journal of Intelligent Material Systems and Structures Structures 31, 1731–1747.

Routh, E.J., 1877. A treatise on the stability of a given state of motion, particularly steady motion. Macmillan and Co., London (UK).

Seba, B., Ni, J., Lohmann, B., 2006. Vibration attenuation using a piezoelectric shunt circuit based on finite element method analysis. Smart Materials and Structures 15, 509–517.

Soltani, P., Kerschen, G., Tondreau, G., Deraemaeker, A., 2017. Tuning of a piezoelectric vibration absorber attached to a damped structure. Journal of Intelligent Material Systems and Structures 28, 1115–1129.

Sun, H., Yang, Z., Li, K., Li, B., Xie, J., Wu, D., Zhang, L., 2009. Vibration suppression of a hard disk driver actuator arm using piezoelectric shunt damping with a topology-optimized PZT transducer. Smart Materials and Structures 18, 065010.

Thomas, O., Deü, J., Ducarne, J., 2009. Vibrations of an elastic structure with shunted piezoelectric patches: efficient finite element formulation and electromechanical coupling coefficients. International Journal for Numerical Methods in Engineering 80, 235–268.

Thomas, O., Ducarne, J., Deü, J.-F., 2012. Performance of piezoelectric shunts for vibration reduction. Smart Materials and Structures 21, 015008.

Thomas, O., Touzé, C., Chaigne, a., 2003. Asymmetric non-linear forced vibrations of free-edge circular plates. Part II: experiments. Journal of Sound and Vibration 265, 1075–1101.

Toftekaer, J.F., Hogsberg, J., 2019. Multi-mode piezoelectric shunt damping with residual mode correction by evaluation of modal charge and voltage. Journal of Intelligent Material Systems and Structures 31, 570–586.

Wu, S., 1996. Piezoelectric shunts with a parallel R-L circuit for structural damping and vibration control. In: SPIE Proceedings - Smart Structures and Materials. San Diego (USA), pp. 259–269.

Xie, F., Su, Y., Zhou, W., Zhang, W.Z., 2019. Design and evaluation of a shunted flexible piezoelectric damper for vibration control of cable structures. Smart Materials and Structures 28.

Yamada, K., Matsuhisa, H., Utsuno, H., Sawada, K., 2010. Optimum tuning of series and parallel LR circuits for passive vibration suppression using piezoelectric elements. Journal of Sound and Vibration 329, 5036–5057.

Zhou, B., Thouverez, F., Lenoir, D., 2014. Vibration Reduction of Mistuned Bladed Disks by Passive Piezoelectric Shunt Damping Techniques. AIAA Journal 52, 1194–1206.